Journal of the Korean Crystal Growth and Crystal Technology
Vol. 32, No. 1 (2022) 16-24
https://doi.org/10.6111/JKCGCT.2022.32.1.016

p-ISSN 1225-1429
e-ISSN 2234-5078

Heat transfer study of double diffusive natural convection in a two-dimensional enclosure at different aspect ratios and thermal Grashof number during the physical vapor transport of mercurous bromide (Hg_2Br_2): Part I. Heat transfer

Sung Ho Ha and Geug Tae Kim†

Department of Chemical Engineering, Hannam University, Daejeon 34054, Korea

(Received January 18, 2022)
(Revised January 25, 2022)
(Accepted January 27, 2022)

Abstract A computational study of combined thermal and solutal convection (double diffusive convection) in a sealed crystal growth reactor is presented, based on a two-dimensional numerical analysis of the nonlinear and strongly coupled partial differential equations and their associated boundary conditions. The average Nusselt numbers for the source regions are greater than those at the crystal regions for $9.73 \times 10^3 \le Gr_t \le 6.22 \times 10^5$. The average Nusselt numbers for the source regions varies linearly and increases directly with the thermal Grashof number form $9.73 \times 10^3 \le Gr_t \le 6.22 \times 10^5$ for aspect ratio, Ar (transport length-to-width) = 1 and 2. Additionally, the average Nusselt numbers for the crystal regions at Ar = 1 are much greater than those at Ar = 2. Also, the occurrence of one unicellular flow structure is caused by both the thermal and solutal convection, which is inherent during the physical vapor transport of Hg_2Br_2. When the aspect ratio of the enclosure increases, the fluid movement is hindered and results in the decrease of thermal buoyancy force.

Key words Physical vapor transport, Hg_2Br_2

1. Introduction

Recently, there has been drawn much attention in the applications of acousto-optic materials and signal processing optics for thallium arsenic selenide (Tl_3AsSe_3), and mercurous chloride (Hg_2Cl_2) and mercurous bromide (Hg_2Br_2), which leads to extensive research works [1-10].

One of the important topics in material processing is the combined thermal and solutal convection, i.e., double diffusive convection which occurs inherently due to the driving forces of temperature and solutal gradients on earth. Yang and Zhao [11] investigated a two-dimensional computational study of double-diffusive convection in rectangular enclosures with various geometries and Liu et al. [12] carried out numerically the importance of the Dufour and Soret effects utilizing multiple-relaxation-time lattice Boltzmann model in double diffusive convection systems. Chakkingal et al. [13] examined the flow regimes in a cubical enclosure with adiabatic cylindrical obstacle, and Meften [14] performed the study of double diffusive convection from a point of view of conditional stability. More recently, Hamimid et al. [15] studied on the importance of limit of the buoyancy effect for double-diffusive convection and Chauhan et al. [16] reported the influence of viscous dissipation on thermo-solutal convection in a square enclosure. Kim et al. [17-20] have performed computational study of combined thermal and solutal convection of mercurous chloride and mercurous bromide vapors in the sealed crystal growth reactors. Weaver and Viskanta [21] investigated diffusive-advection convection with the out of mass flux at the hot walls and the in of mass flux at the cold walls in two-dimensional rectangular enclosures.

In this study, a computational study of combined thermal and solutal convection (double diffusive convection) in a sealed crystal growth reactor is presented, based on a two-dimensional numerical analysis of the nonlinear and strongly coupled partial differential equations and their associated boundary conditions with a compressible model of ideal gas law. A computational study of velocity vectors and streamlines, isotherms and iso-mass concentrations is performed for $\Delta T = 20^oC$, the temperature difference between the source (350^oC) and crystal regions (330^oC), the partial pressures of component argon of 20 Torr.

2. Analysis

We consider the PVT (physical vapor transport) crys-

†Corresponding author
E-mail: geugtaekim@gmail.com

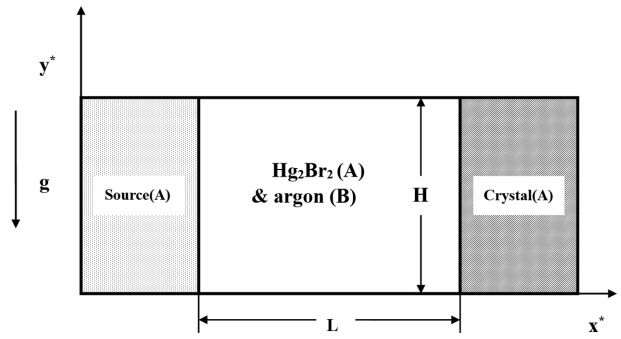

Fig. 1. System schematic descriptions and coordinates for two-dimensional numerical simulations of a PVT crystal growth enclosure of major component Hg_2Br_2 (A) and impurity argon (B).

tal growth in a two-dimensional enclosure, as shown in Fig. 1. The two-dimensional configuration is a square enclosure of aspect ratio, Ar = 1 and an enclosure of aspect ratio, Ar = 2, with one vertical surface maintained at high temperature, referred as a source region, and with the opposite vertical wall kept at low temperature, referred as a crystal region. Hg_2Br_2 (species A) at the source region is transported into at crystal region. Argon (species B) as an inert carrier gas, insoluble in Hg_2Br_2 (species A) exists in the vapor phase within the enclosure. Analysis is achieved for the mathematical model for double diffusive natural convection system based on the following assumptions:

- The fluid is assumed be Newtonian and incompressible.
- The fluid is assumed to be laminar.
- The flow is assumed to be two-dimensional and independent of time.
- The fluid is assumed to behave as a continuum and to be no slip at the walls.
- The thermo-physical properties of the fluid except the density variation in the buoyancy term are considered to be constant. The density depends on the perfect gas law.
- Radiation, viscous dissipation effects are assumed to be negligible.

2.1. Dimensionless form of equations

The dimensionless quantities are:

$x^* = x/H$, $y^* = y/H$, $u = v_x/U$, $v = v_y/U$, $p^* = p/\rho_0 U^2$, $T^* = (T - T_c)/(T_h - T_c)$, $\omega^*_{A,} = (\omega_A - \omega_{A,c})/(\omega_{A,s} - \omega_{A,c})$, $U = \alpha/H$,

where x, y are rectangular coordinate along the transport length and the height of the enclosure, respectively, and p is the pressure. The U is the characteristic velocity and H is the height of the enclosure. The dimensionless parameters (Prandtl number, Pr; Lewis number, Le; Grashof number, Gr) in the following governing equations can be found in reference [22]. The β is the coefficient of thermal volume expansion. The mass concentration ω_A is defined as $\omega_A = \frac{x_A M_A}{x_A M_A + x_B M_B}$, x is mole fraction of component A, M is the number-mean molecular weight of mixture.

By applying the dimensionless variables, the governing equations can be expressed by non-dimensionless form:

$$\nabla^* \cdot \vec{V} = 0, \tag{1}$$

$$\vec{V} \cdot \nabla^* \vec{V} = -\nabla^* p^* + \mathrm{Pr}\nabla^{*2}\vec{V} - \mathrm{Gr} \cdot \mathrm{Pr}^2 \frac{(1 - \rho^*)}{\beta \Delta T,} \tag{2}$$

$$\vec{V} \cdot \nabla^* T^* = \nabla^{*2} T^*, \tag{3}$$

$$\vec{V} \cdot \nabla^* \omega_A^* = \frac{1}{\mathrm{Le}} \nabla^{*2} \omega_A^*. \tag{4}$$

The associated boundary conditions are given as follows:

On the walls
$(0 < x^* < 1, y^* = 0 \text{ and } 1)$:

$$u(x^*, 0) = u(x^*, 1) = v(x^*, 0) = v(x^*, 1) = 0 \tag{5}$$

$$\frac{\partial \omega_A^*(x^*, 0)}{\partial y^*} = \frac{\partial \omega_A^*(x^*, 1)}{\partial y^*} = 0,$$

$$T^*(x^*, 0) = -x^* + 1.$$

On the source $(x^* = 0, 0 < y^* < 1)$:

$$u(0, y^*) = -\frac{1}{\mathrm{Le}(C_v - 1)} \frac{\partial \omega_A^*(0, y^*)}{\partial x^*}, \tag{6}$$

$$v(0, y^*) = 0,$$
$$T^*(0, y^*) = 1,$$
$$\omega_A^*(0, y^*) = 1.$$

On the crystal $(x^* = 1, 0 < y^* < 1)$:

$$u(1, y^*) = -\frac{1}{\mathrm{Le}(C_v - 1)} \frac{\partial \omega_A(1, y)}{\partial x^*}, \tag{7}$$

$$v(1, y^*) = 0,$$
$$T^*(1, y^*) = 1,$$
$$\omega_A^*(1, y^*) = 1.$$

The heat transfer of the diffusive-convection in the enclosure can be expressed in terms of the local Nu_y, from the definition of dimensionless Nusselt number,

$Nu_y = hH/k$ and the average convective Nusselt $Nu = -\int Nu_y\,(y^*)\,dy^*$. When Q_d illustrates the increased heat transfer at the wall due to double-diffusive convection and $Q_a = \rho^* u T^*$ is the dimensionless energy flux due to advection, the total energy transferred at the wall is expressed by $Nu = Q_d + Q_a$ [21].

2.2. Method of solution

The numerical investigation utilized the Semi-Implicit Method Pressure-Linked Equations Revised (SIMPLER) [23] iterative technique for the two-dimensional case for heat transfer Grashof numbers ranged from 9.73×10^3 to 6.22×10^5.

3. Results and Discussion

When the molecular weight of Hg_2Br_2 ($M_A = 560.988$ g/gmol) is not equal to the molecular weight of argon ($M_B = 39.944$ g/gmol), i.e., $M_A \neq M_B$, the transport phenomena in the vapor phase during the physical vapor transport (PVT) are much complicated because of both thermal and solutal buoyancy driven natural convection and the mass flux of Hg_2Br_2 (A) in the source and crystal interfaces. Table 1 lists up the average Nusselt numbers for the heat transfer study of double diffusive natural convection in a two-dimensional enclosure at different aspect ratios and thermal Grashof number during the physical vapor transport of mercurous bromide (Hg_2Br_2). Table 2 shows in details that the average Nusselt numbers at the source and crystal interfaces due to the diffusive-convection and the advection, corresponding to Table 1. The typical process parameter used in this study can be found in reference [22].

Figure 2 shows the average Nusselt numbers for the crystal regions, Nu_c as a function of the thermal Grashof number (Gr_t) at two different aspect ratios, $Ar = 1$ and 2. As shown in Fig. 2, Nu_c varies linearly and increases directly with the thermal Grashof number form $9.73 \times 10^3 \le Gr_t \le 6.22 \times 10^5$ for Ar (transport length-to-width, L/H) = 1 and 2. Additionally, the average Nus-

Table 1
The average Nusselt numbers for the heat transfer study of double diffusive natural convection in a two-dimensional enclosure at different aspect ratios and thermal Grashof numbers during the physical vapor transport of mercurous bromide (Hg_2Br_2)

Case	Thermal Grashof number, Gr_t	Prandtl number, Pr	Aspect ratio (transport length-to-width, L/H), Ar	Average Nusselt number (source region), Nu_s	Average Nusselt number (crystal region), Nu_c	$\|U\|_{max}$ (cm/s)
C1	9.73×10^3	0.99	1.0	45.4	44.8	10.4
C2	7.78×10^4	0.99	1.0	83.9	85.1	13.4
C3	2.62×10^5	0.99	1.0	117.6	118.0	16.5
C4	6.22×10^5	0.99	1.0	149.2	145.6	19.6
C5	9.73×10^3	0.99	2.0	32.6	15.4	3.20
C6	7.78×10^4	0.99	2.0	76.1	48.1	4.57
C7	2.62×10^5	0.99	2.0	117.0	79.9	5.67
C8	6.22×10^5	0.99	2.0	155.6	106.9	6.72

Table 2
The average Nusselt numbers at the source and crystal interfaces due to the diffusive-convection and the advection, corresponding to Table 1

Case	Average Nusselt number (source region), Nu_s			Average Nusselt number (crystal region), Nu_c		
	Dimensionless diffusive-convection energy flux, Q_d	Dimensionless energy flux due to advection, Q_a	Total ($Q_d + Q_a$)	Dimensionless diffusive-convection energy flux, Q_d	Dimensionless energy flux due to advection, Q_a	Total ($Q_d + Q_a$)
C1	0.06	45.4	45.4	27.6	17.2	44.8
C2	0.04	83.9	83.9	41.5	43.6	85.1
C3	0.04	117.6	117.6	50.4	67.6	118.0
C4	0.04	149.2	149.2	56.8	88.8	145.6
C5	0.07	32.6	32.6	8.3	7.1	15.4
C6	0.04	76.1	76.1	16.8	31.4	48.1
C7	0.03	117.0	117.0	22.5	57.4	79.9
C8	0.03	155.6	155.6	26.2	80.7	106.9

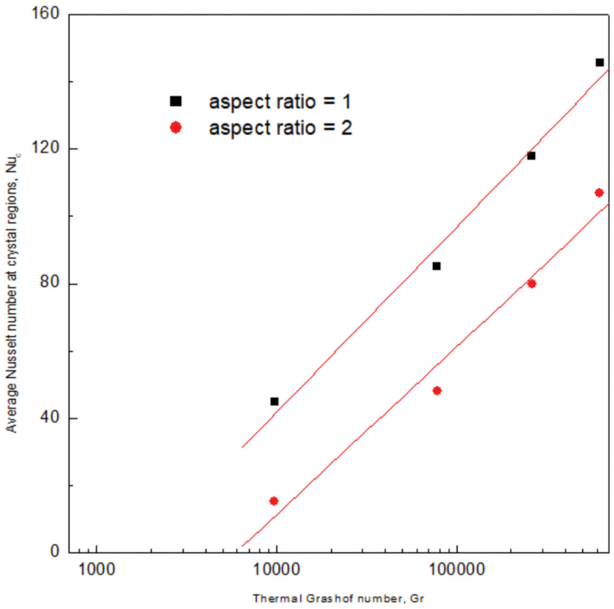

Fig. 2. The average Nusselt numbers for the crystal regions as a function of the thermal Grashof number at two different aspect ratios, Ar = 1 and 2.

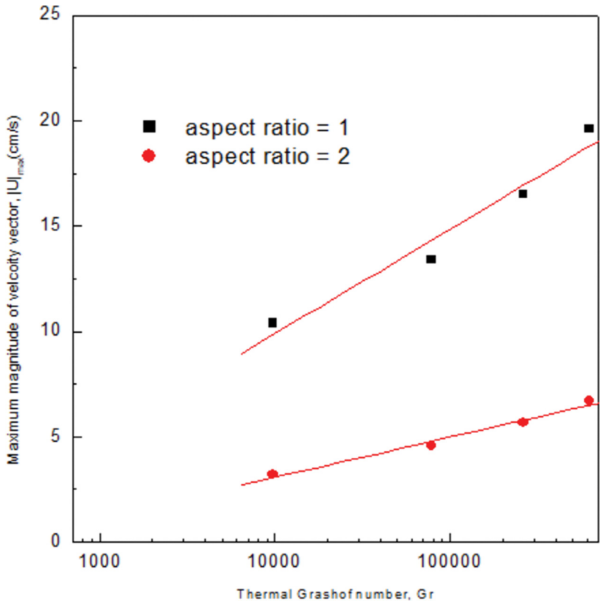

Fig. 4. The maximum magnitudes of velocity vector, $|U|_{max}$ as a function of the thermal Grashof number at two different aspect ratios, Ar = 1 and 2.

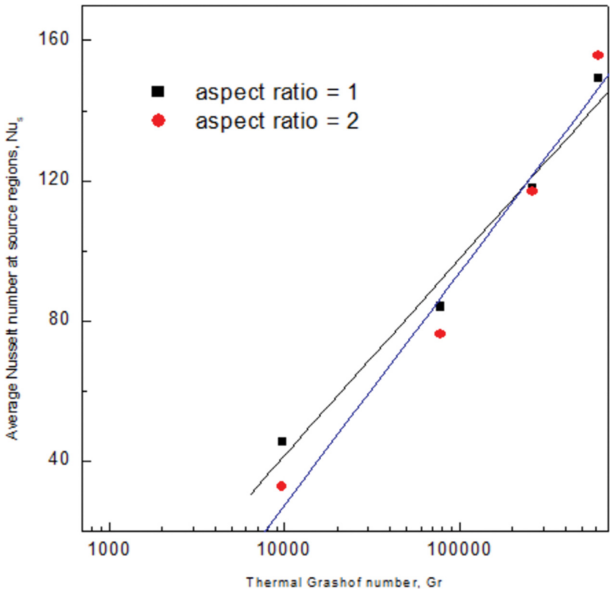

Fig. 3. The average Nusselt numbers for the source regions as a function of the thermal Grashof number at two different aspect ratios, Ar = 1 and 2.

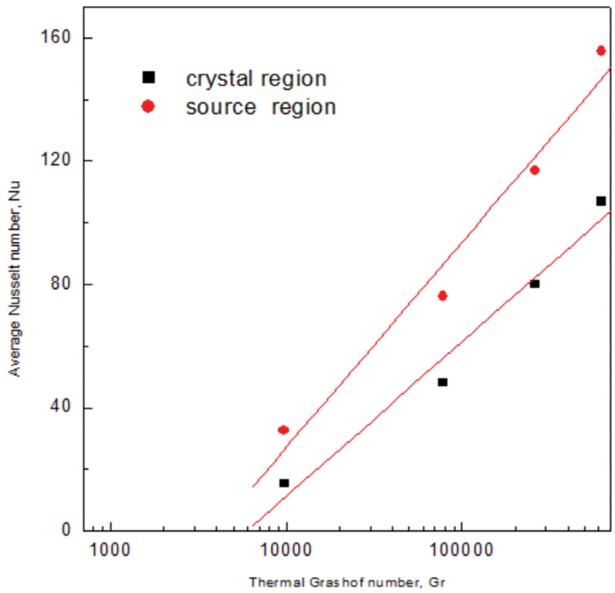

Fig. 5. The average Nusselt numbers for both the crystal and the source regions as a function of the thermal Grashof number at the aspect ratio of 2, Ar = 2.

selt numbers for the crystal regions at Ar = 1 are much greater than those at Ar = 2. Figure 3 shows the average Nusselt numbers for the source regions, Nu_s, as a function of the thermal Grashof number at two different aspect ratios, Ar = 1 and 2. Like the case of the average Nusselt numbers for the crystal regions, Nu_c, the average Nusselt numbers for the source regions, Nu_s varies linearly and increases directly with the thermal Grashof number form $9.73 \times 10^3 \le Gr_t \le 6.22 \times 10^5$ for Ar (transport length-to-width, L/H) = 1 and 2. Note that the average Nusselt numbers for the source regions at Ar = 1 are greater than those at Ar = 2 for $9.73 \times 10^3 \le Gr_t \le 7.78 \times 10^4$, but that the average Nusselt numbers for the source regions at Ar = 2 is greater than those at Ar = 1 for $2.62 \times 10^5 \le Gr_t \le 6.62 \times 10^5$. At this time, the reason of this finding is not clear considering the comparisons of

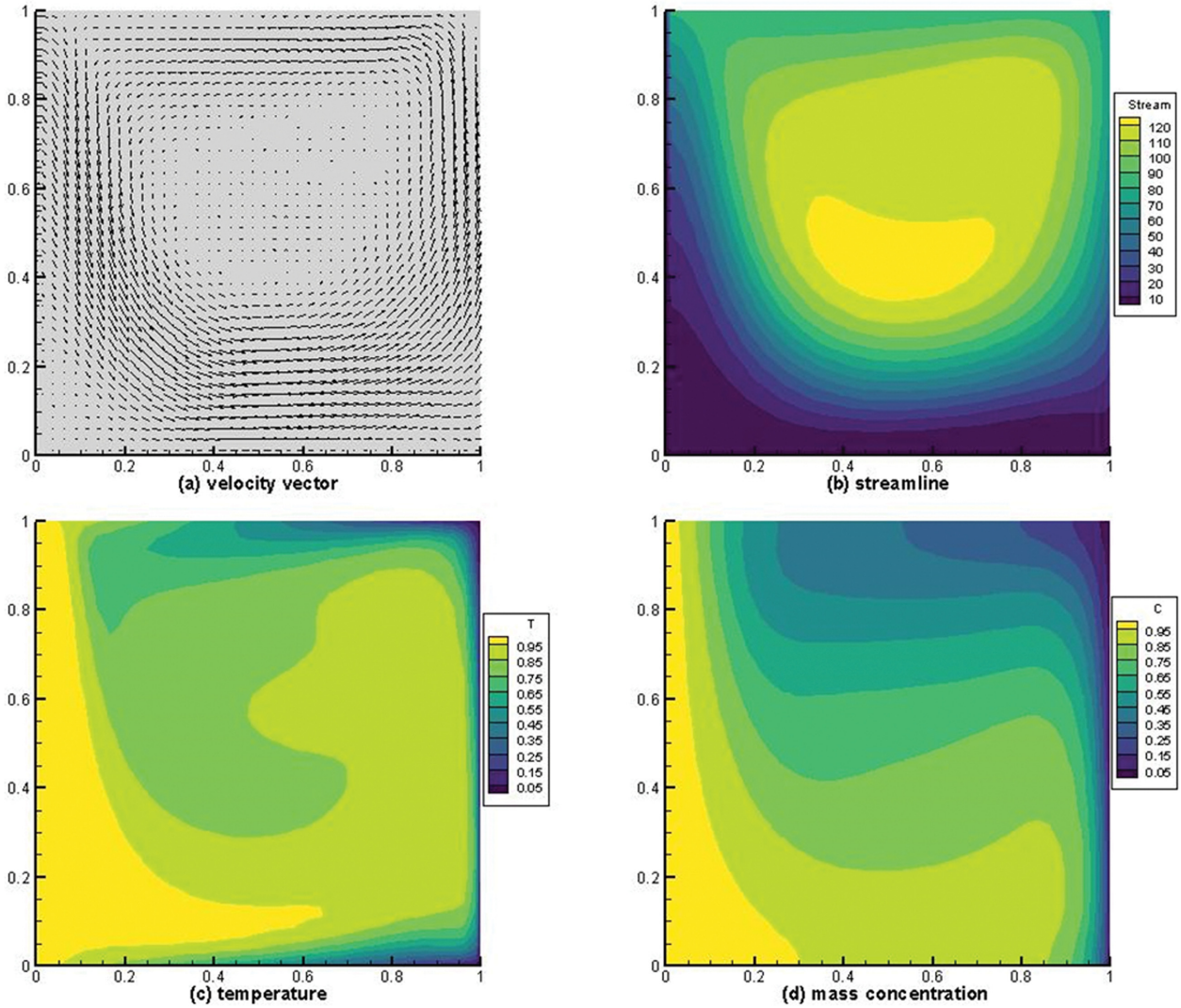

Fig. 6. (a) velocity vector fields ($|U|_{max}$ = 13.4 cm/s), (b) streamlines (ψ_{min} = 0, ψ_{max} = 124.4, $\delta\psi$ = 10), (c) isotherms (δT^* = 0.1), (d) iso-mass concentrations ($\delta\omega^*$ = 0.1), for the heat transfer case, Table 1, case C2 with thermal Grashof number (Gr_t) = 7.78×10^4, aspect ratio (Ar) = 1.

maximum magnitudes of velocity vectors.

Figure 4 shows the maximum magnitudes of velocity vector, $|U|_{max}$ as a function of the thermal Grashof number at two different aspect ratios, Ar = 1 and 2. The maximum magnitudes of velocity vector, $|U|_{max}$ increases directly and linearly with the thermal Grashof number form $9.73 \times 10^3 \le Gr_t \le 6.22 \times 10^5$ for Ar (transport length-to-width, L/H) = 1 and 2. The $|U|_{max}$ at Ar = 1 are much greater than those at Ar = 2 by a factor of 3. This finding reflects the effect of walls along the transport length. The thermal Grashof number for the case C4 ($|U|_{max}$ = 19.6 cm/sec), is greater one order of magnitude than that for the case C2, but, from the comparisons of the maximum magnitudes of the velocity vector, $|U|_{max}$, indicative of the contribution of thermal convection, it is concluded that the maximum magnitudes of the velocity vector, $|U|_{max}$ is increased with the thermal Grashof number by 50%. The detailed flow characteristics of cases C2 and C4 are presented in Figs. 6 and 7, respectively.

Figure 5 shows the average Nusselt numbers for both the crystal and the source regions as a function of the thermal Grashof number at the aspect ratio of 2, Ar = 2. As shown in Fig. 5, it is found that the average Nusselt numbers for the source regions are greater than those at the crystal regions for $9.73 \times 10^3 \le Gr_t \le 6.22 \times 10^5$.

Figure 6 shows the velocity vector fields ($|U|_{max}$ = 13.4 cm/sec), streamlines (ψ_{min} = 0, ψ_{max} = 124.4, $\delta\psi$ = 10), isotherms (δT^* = 0.1), iso-mass concentrations ($\delta\omega^*$ = 0.1), for the heat transfer case, Table 1, case C2 with thermal Grashof number (Gr_t) = 7.78×10^4, aspect ratio = 1. As shown in Fig. 6, one convection cell appears and seems asymmetrical against the mid-transport length

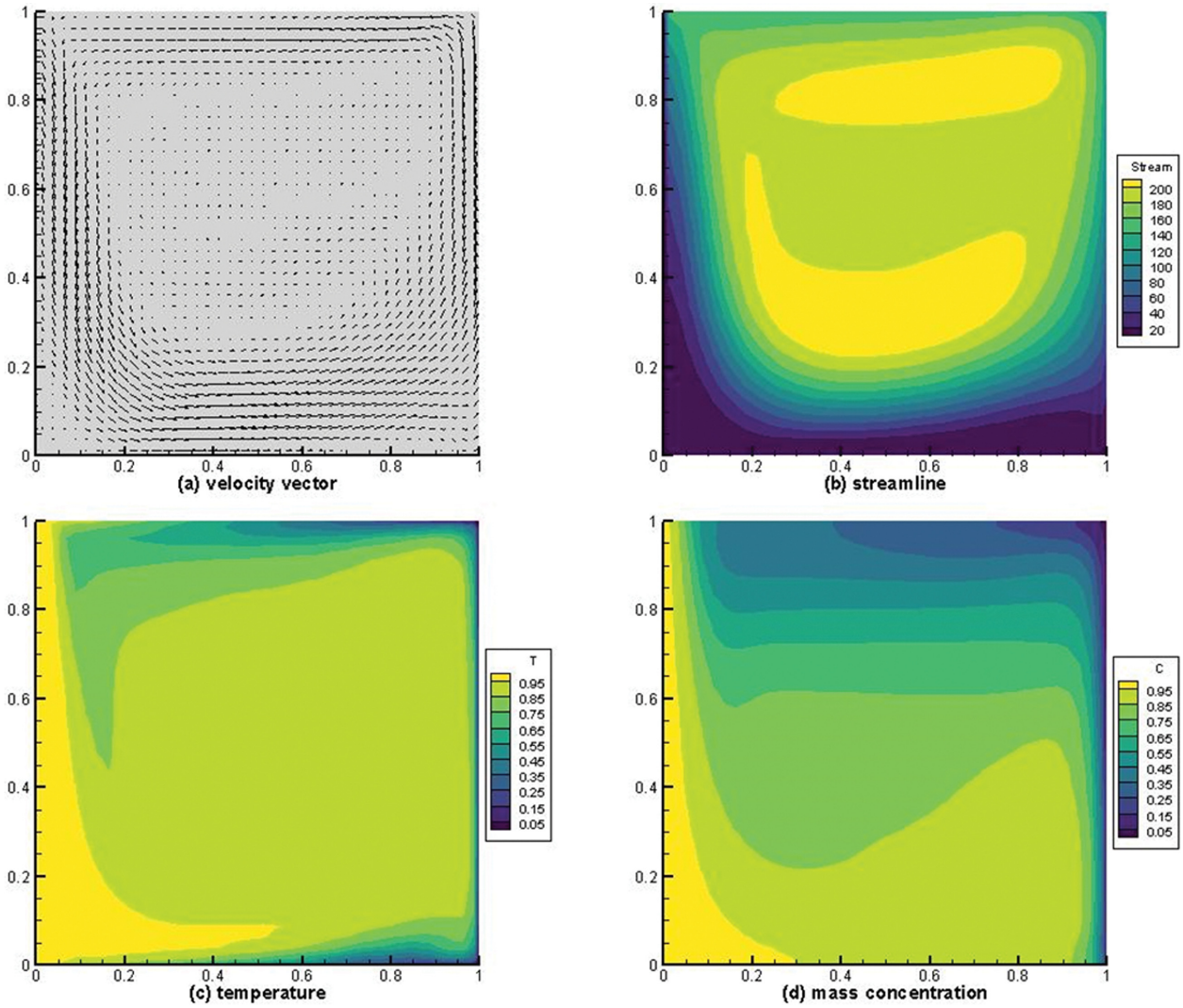

Fig. 7. (a) velocity vector fields ($|U|_{max}$ = 19.6 cm/s), (b) streamlines (ψ_{min} = –1.3, ψ_{max} = 217.5, $\delta\psi$ = 10), (c) isotherms (δT^* = 0.1), (d) iso-mass concentrations ($\delta\omega^*$ = 0.1), for the heat transfer case, Table 1, case C4 with thermal Grashof number (Gr_t) = 6.22×10^5, aspect ratio (Ar) = 1.

of the enclosure (x^* = 0.5). Figure 7 is concerned with the heat transfer case, Table 1, case C4 with thermal Grashof number (Gr_t) = 6.22×10^5, aspect ratio = 1. As shown in Figs. 6 and 7, the temperature and mass concentration gradients in the vertical walls near the crystal regions are greater than those in the horizontal walls near the crystal regions. Figures 6 and 7 indicate the presence of velocity boundary layers along the crystal regions.

Figures 8 and 9 show the velocity vector fields, streamlines, isotherms, iso-mass concentrations, for the heat transfer case, Table 1, cases C6 and C8, aspect ratio = 2, respectively. Figures 8 and 9 illustrate the presence of velocity boundary layers along the bottom walls and crystal regions. The effect of the aspect ratio may be illustrated by comparing the flow structure characteristics of the velocity vector fields, streamlines, isotherms, iso-mass concentrations, i.e., (1) the case of Figs. 6 and 8 for the fixed thermal Grashof number of 7.78×10^4, (2) the case of Figs. 7 and 9 for the fixed thermal Grashof number of 6.22×10^5. As shown in Figs. 6 through 9, the occurrence of one unicellular flow structure is caused by both the thermal and solutal convection, which is inherent during the physical vapor transport of Hg_2Br_2. Comparisons of one case of Figs. 6 and 8, and the other case of Figs. 7 and 9 show that the convective flow structure is stabilized and the maximum magnitude of velocity vector decreases with increasing the aspect ratio, which is related to the wall effects. In other words, Increasing the aspect ratio of the enclosure results in the hindrance of the fluid movement and the reduction of thermal buoyancy force.

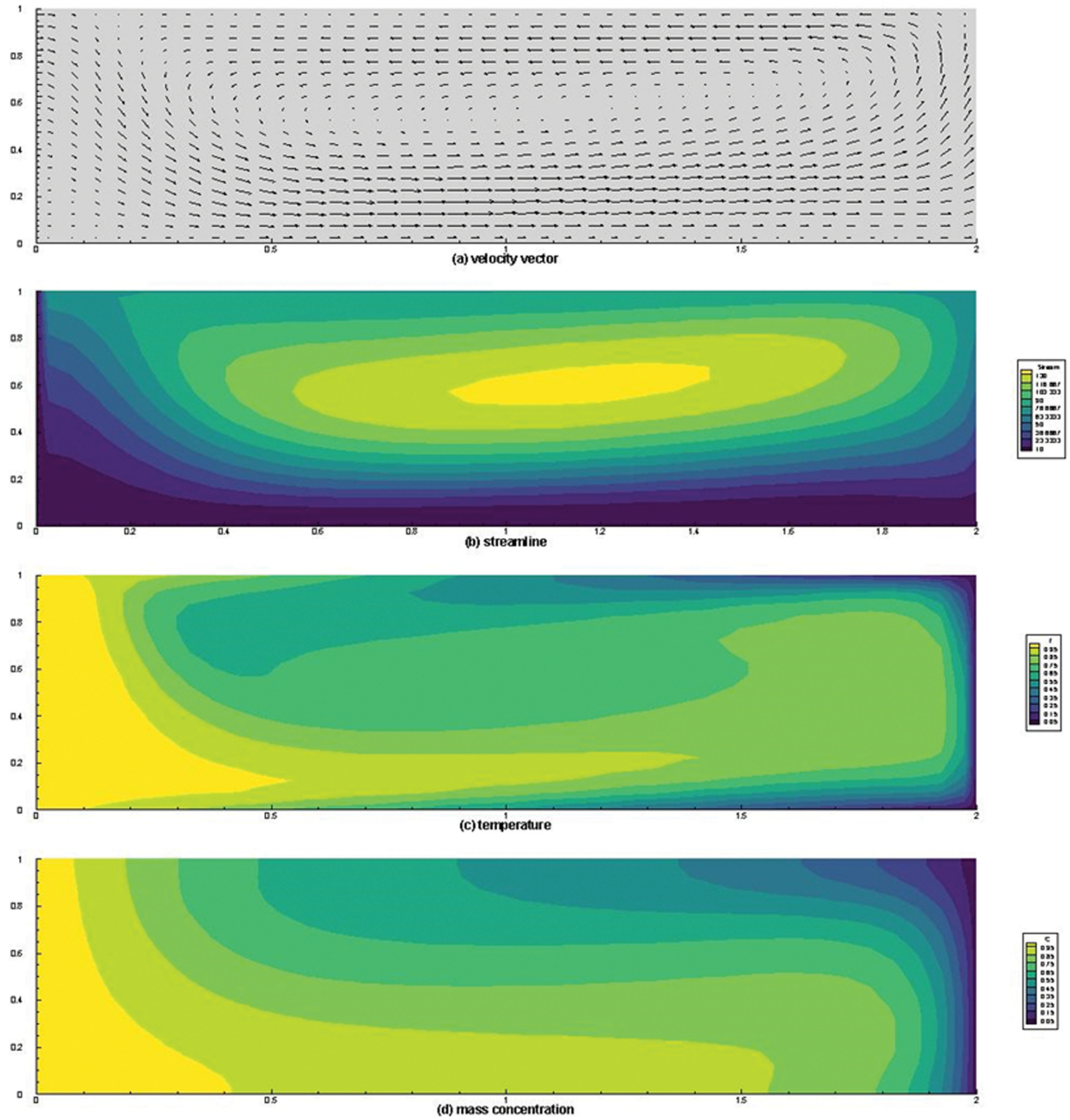

Fig. 8. (a) velocity vector fields ($|U|_{max} = 4.57$ cm/s), (b) streamlines ($\psi_{min} = 0$, $\psi_{max} = 124.4$, $\delta\psi = 10$), (c) isotherms ($\delta T^* = 0.1$), (d) iso-mass concentrations ($\delta\omega^* = 0.1$), for the heat transfer case, Table 1, case C6 with thermal Grashof number (Gr_t) = 7.78×10^4, aspect ratio (Ar) = 2.

4. Conclusions

In conclusions, the average Nusselt numbers for the source regions are greater than those at the crystal regions for $9.73 \times 10^3 \le Gr_t \le 6.22 \times 10^5$. The average Nusselt numbers for the source regions varies linearly and increases directly with the thermal Grashof number form $9.73 \times 10^3 \le Gr_t \le 6.22 \times 10^5$ for Ar (transport length-to-width, L/H) = 1 and 2. Additionally, the average Nusselt numbers for the crystal regions at Ar = 1 are much greater than those at Ar = 2. Also, the occurrence of one unicellular flow structure is caused by both the thermal and solutal convection, which is inherent during the physical vapor transport of Hg_2Br_2. When the aspect ratio of the enclosure increases, the movement of fluid is retarded and results in the decrease of thermal buoy-

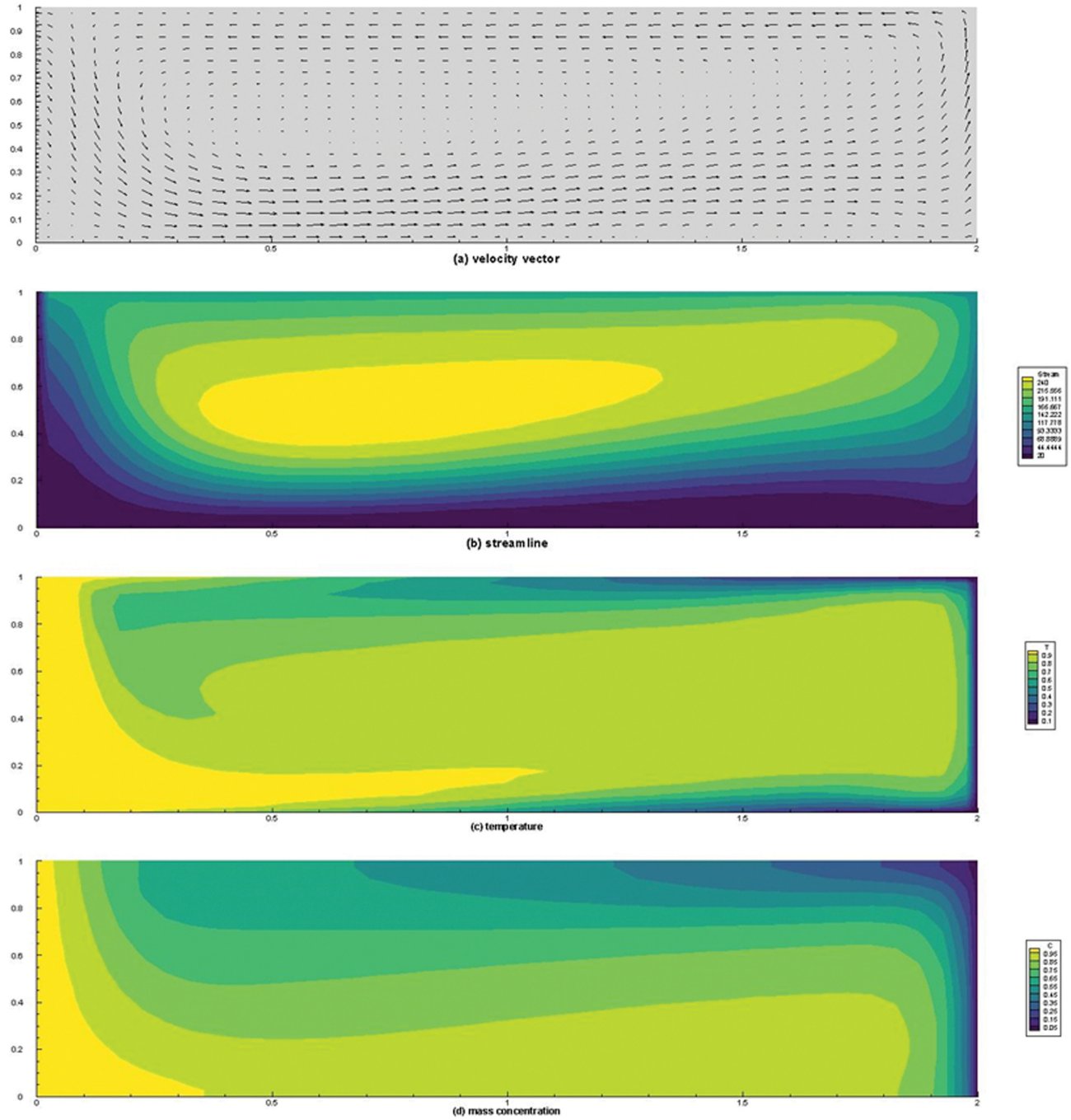

Fig. 9. (a) velocity vector fields ($|U|_{max} = 6.72$ cm/s), (b) streamlines ($\psi_{min} = 0$, $\psi_{max} = 124.4$, $\delta\psi = 10$), (c) isotherms ($\delta T^* = 0.1$), (d) iso-mass concentrations ($\delta\omega^* = 0.1$), for the heat transfer case, Table 1, case C8 with thermal Grashof number (Gr_t) = 6.62×10^5, aspect ratio (Ar) = 2.

ancy force.

Acknowledgement

This work was financially supported by the 2019 Hannam University Research Fund under Grant No. 2019A114 (April 1, 2019 through March 31, 2020).

References

[1] A.A. Kaplyanskii, V.V. Kulakov, Yu.F. Markov and Ĉ. Barta, "The soft mode properties in Raman spectra of improper ferroelastics Hg_2Cl_2 and Hg_2Br_2", Solid State Commun. 21 (1977) 1023.

[2] M. Dalmon, S. Nakashima, S. Komatsubara and A. Mitsuishi, "Softening of acoustic and optical modes in ferroelstic phase in Hg_2Br_2", Solid State Commun. 28

(1978) 815.
[3] N.B. Singh, M. Gottlieb, A.P. Goutzoulis, R.H. Hopkins and R. Mazelsky, "Mercurous Bromide acousto-optic devices", J. Cryst. Growth 89 (1988) 527.
[4] N.B. Singh, M. Gottlieb, G.B. Branddt, A.M. Stewart, R.H. Hopkins, R. Mazelsky and M.E. Glicksman, "Growth and characterization of mercurous halide crystals: mercurous bromide system", J. Cryst. Growth 137 (1994) 155.
[5] J.S. Kim, S.B. Trivedi, J. Soos, N. Gupta and W. Palosz, "Growth of Hg_2Cl_2 and Hg_2Br_2 single crystals by physical vapor transport", J. Cryst. Growth 310 (2008) 2457.
[6] P.M. Amarasinghe, J.S. Kim, H. Chen, S. Trivedi, S.B. Qadri, J. Soo, M. Diestler, D. Zhang, N. Gupta and J.L. Jensen, "Growth of high quality mercurous halide sing crystals by physical vapor transport method for AOM and radiation detection applications", J. Cryst. Growth 450 (2016) 96.
[7] T.H. Kim, H.T. Lee, Y.M. Kang, G.E. Jang, I.H. Kwon and B. Cho, "In-depth investigation of Hg_2Br_2 crystal growth and evolution", Materials 12 (2019) 4224.
[8] O. Kwon, K. Kim, S.-G. Woo, G.-E. Jang and B. Cho, "Comparative analysis of Hg_2Br_2 and $Hg_2Br_xCl_{2-x}$ crystals grown via PVT", Crystals 10 (2020) 1096.
[9] L. Liu, R. Li, L. Zhang, P. Zhang, G. Zhang, S. Xia and X. Tao, "Long wavelength infrared acousto-optic crystal Hg_2Br_2: Growth optimization and photosensitivity investigation", J. Alloys Compd. 874 (2021) 159943.
[10] P.M. Amarasinghe, JS. Kim and S. Trivedi "Mercurous Bromide (Hg_2Br_2) Acousto-Optic Tunable Filters (AOTFs) for the Long Wavelength Infrared (LWIR) Region", J. Electron. Mater. 50 (2021) 5774.
[11] J.-Q. Yang and B.-X. Zhao, "Numerical investigation of double-diffusive convection in rectangular cavities with different aspect ratio I: High-accuracy numerical method", Comput. Math. Appl. 94 (2021) 155.
[12] Q. Liu, X.-B. Feng, X.-T. Xu and Y.-L. He, "Multiple-relaxation-time lattice Boltzmann model for double-diffusive convection with Dufour and Soret effects", Int. J. Heat Mass Transf. 139 (2019) 713.
[13] M. Chakkingal, R. Voigt, C.R. Kleijn and S. Kenjereš, "Effect of double-diffusive convection with cross gradients on heat and mass transfer in a cubical enclosure with adiabatic cylindrical obstacles", Int. J. Heat Fluid Flow 83 (2020) 108574.
[14] G.A. Meften, "Conditional and unconditional stability for double diffusive convection when the viscosity has a maximum", Appl. Math. Comput. 392 (2021) 125694.
[15] S. Hamimid, M. Guellal and M. Bouafia, "Limit the buoyancy ratio in Boussinesq approximation for double-diffusive convection in binary mixture", Phys. Fluids 33 (2021) 036101.
[16] A. Chauhan, P.M. Sahu and C. Sasmal, "Effect of polymer additives and viscous dissipation on natural convection in a square cavity with differentially heated side walls", Int. J. Heat and Mass Transf. 175 (2021) 121342.
[17] G.T. Kim and M. H. Kwon, "Effects of solutally dominant convection on physical vapor transport for a mixture of Hg_2Br_2 and Br_2 under microgravity environments", Korean Chem. Eng. Res. 52 (2014) 75.
[18] G.T. Kim and M.H. Kwon, "Numerical analysis of the influences of impurity on diffusive-convection flow fields by physical vapor transport under terrestrial and microgravity conditions: with application to mercurous chloride", Appl. Chem. Eng. 27 (2016) 335.
[19] S.H. Ha and G.T. Kim, "Preliminary studies on double-diffusive natural convection during physical vapor transport crystal growth of Hg_2Br_2 for the spaceflight experiments", Korean Chem. Eng. Res. 57 (2019) 289.
[20] G.T. Kim and M.H. Kwon, "Double-diffusive convection affected by conductive and insulating side walls during physical vapor transport of Hg_2Br_2", J. Korean Cryst. Growth Cryst. Tech. 30 (2020) 117.
[21] J.A. Weaver and R. Viskanta, "Natural convection due to horizontal temperature and concentration gradients -1. Variable thermophysical property effects", Int. J. Heat and Mass Transf. 34 (1991) 3107.
[22] G.T. Kim and M.H. Kwon, "Studies on Nusselt and Sherwood number for diffusion-advective convection during physical vapor transport of Hg_2Br_2", J. Korean Cryst. Growth Cryst. Tech. 31 (2021) 127.
[23] S.V. Patankar, "Numerical Heat Transfer and Fluid Flow" (Hemisphere Publishing Corp., Washington D. C., 1980) p. 131.